ACS OMEGA

http://pubs.acs.org/journal/acsodf

Article

New Tailored RNA-Targeted Organometallic Drug Candidates against Huh7 (Liver) and Du145 (Prostate) Cancer Cell Lines

Huzaifa Yasir Khan, Santosh K. Maurya, Hifzur R. Siddique, Shariq Yousuf, and Farukh Arjmand*

Cite This: *ACS Omega* 2020, 5, 15218−15228

Read Online

ACCESS | Metrics & More | Article Recommendations | Supporting Information

ABSTRACT: New organometallic drug candidates [$Ph_2Sn(HL)$], **1**, and [Ru(η^6--*p*-cymene)(HL)Cl], **2**, were designed and synthesized by in situ reaction of a Schiff base ligand (HL) and diphenyltin dichloride and [$RuCl_2$(*p*-cymene)]$_2$, respectively. The drug candidates **1** and **2** have been characterized by spectroscopic methods (Fourier-transform infrared spectroscopy, UV−vis, and $^1H/^{13}C$ NMR), elemental analysis, and single X-ray crystallographic studies (in case of **1**). The ground-state geometry optimization of **1** and **2** was performed by density functional theory calculations. The interaction of **1** and **2** with tRNA was assessed by absorption spectroscopy, cyclic voltammetry, circular dichroism, and ethidium bromide displacement assay using fluorescence emission spectroscopy to determine their potential to act as antitumor agents. The cytotoxicity of **1** and **2** was screened against human liver carcinoma (Huh7), prostate cancer (Du145), and the normal prostate cell line (PNT 2). The results implicated a dose-dependent growth inhibition of the two cancer cells at concentrations (2.5−15 μM) of **1** and **2** with the treatment after 48 h. Interestingly, **1** revealed good selective activity toward the liver cancer cell line (Huh7). Furthermore, both the drug candidates **1** and **2** were found to be nontoxic toward the PNT 2 normal cell line. These studies lay a paradigm for rational efficacious drug design for chemotherapeutic intervention in cancers using new tailored organometallic drug entities; organotin(IV) and organoruthenium(II) have been demonstrated to be viable for the safe administration and specific targeted drug uptake by the resistant cancerous cell lines at low intracellular concentrations.

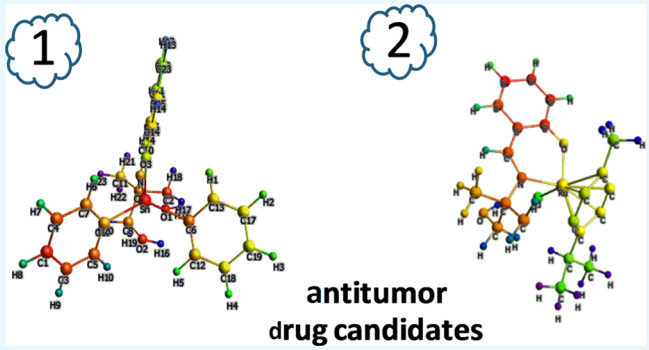

INTRODUCTION

Among the nonplatinum antitumor chemotherapeutic metallodrugs, organometallic compounds, namely, organotin(IV) and organoruthenium{(II) and (III)}, have shown promise to treat solid malignancies. Organometallic compounds exhibit diversity in structure because of their myriad pharmacologically active scaffolds and display their unique properties.[1−4] Organometallics have aroused continued interest in cancer oncology because of these salient features; (i) redox-active and kinetically stable, (ii) better and more effective penetration in tumor cells because of their lipophilic nature, (iii) show ability against resistant cell strains, (iv) possess a specific mode of action against different phenotypes of cancers, and (v) apoptosis inducing nature.[5,6]

Organotin(IV) complexes are known to cause DNA damage by preferential binding to oxygen atoms of the phosphate backbone of a DNA helix and ultimately cell death.[7] Numerous review articles reported the mechanistic pathway of cell death and structure−activity relationship of organotin(IV) derivatives.[8−10] Though the organotin moiety is crucial for cytotoxicity, a ligand framework assumes a vital role in specific targeting and transportation of the molecule to the target site. In the structural formulation, R_nSnL_{4-n}, L has least contribution to the toxicity while R contributes the most. Literature reports from in vivo and in vitro toxicity experiments reveal that the most suitable organotin compounds are those with larger R groups such as triorganotins while R_2SnL_2 and $RSnL_3$ compounds (which are the metabolites of R_3SnL) could be the preferred choice because of the much reduced toxicity.[8,11] Beltrán et al. reported Schiff base complexes of diphenyltin(IV) compounds and evaluated their cytotoxic activity against a panel of human cancer cell strains. The results implicated remarkably good activity with cytospecificity on U251, MCF-7, and SKLU-1 cancer strains at 2.5 μM doses, which were found to be lower than the IC_{50} value of cisplatin. The inhibitory concentration values for the series were found similar to Ph_2SnCl_2, attributed to the presence of Ph_2Sn moiety in the complexes.[12]

Another, notably important class of anticancer drugs which has attracted our attention is organoruthenium com-

Received: March 18, 2020
Accepted: June 10, 2020
Published: June 19, 2020

https://dx.doi.org/10.1021/acsomega.0c01206
ACS Omega 2020, 5, 15218−15228

pounds.[13−15] Several ruthenium compounds exhibit high in vivo and in vitro antitumor activity among which KP1019 and NAMI-A are promising future-generation anticancer drugs in clinical trials.[16] In particular, these drug candidates show high DNA binding affinity and exciting antitumor properties without undesired systemic effects.[17]

Moreover, organometallic half-sandwich Ru(II), Rh(III), and Ir(III) complexes manifested outstanding in vitro and in vivo antineoplastic activity.[18] Organoruthenium-arene complexes having electron-deficient nuclei were promoted by electroporation and actuated apoptosis at 10^{-4} M.[14] Ruthenium complexes such as RAPTA-C (η^6-*p*-MeC_6H_4Pri)Ru(*P*-pta)Cl_2 (pta = 1,3,5-triaza-7-phospha-tricyclo-[3.3.1.1]decane) with η^6-coordinated arene were found to be efficacious anticancer metallodrugs. However, the ruthenium arene ethylenediammine family of compounds [(η^6-C_6H_5Ph)Ru(*N*,*N*-en)Cl]$^+$ (en = 1,2-ethylenediamine) was found to be highly cytotoxic on the A2870 cancer strain with an impressive IC_{50} value equal to 17 μM.[13] Previous literature reports reveal that the cytotoxicity activity could be modulated by incorporating aromatic arene substituents or other bioactive ligand scaffolds such as quinolones, phenyls, flavonols, cymenes,[19] and so forth, which can fine-tune the pharmacological properties of drug candidates. For example, in many Ru(II) paino-stool complexes,[14] the arene and subordinate ligands are known to assume a key role in the anticancer evaluation. Arene is considered as the core building block responsible for enhancing the cytotoxicity, as arene rings are hydrophobic, which can facilitate the arrival of Ru(II) complexes toward cancerous cells. Furthermore, the arene rings regulate the electron distribution of the Ru(II) complex, which influences the stability of the Ru(II) complexes.

Most of the antitumor therapeutic drugs in clinical trials are targeted at DNA, but RNA has recently emerged as a more potential attractive therapeutic target because of its structural diversity. In the recent past, RNA tertiary interactions were confirmed by using NMR and X-ray crystal studies, which showed that RNA has myriad structures like RNA pseudoknots, RNA hair pins, bulge, loops, mismatches in which specific noncovalent electrostatic, groove, and hydrogen bonding interactions can define the folded structures. In the majority of the cases, single-stranded regions of these structures create unique tertiary interactions with many small molecules. Inorganic complexes have generally the advantage of inducing RNA strand scission, which allows direct mapping of their binding sites. There are few reports on RNA-targeted organometallic compounds of ruthenium, though some Ru(phen)$_3^{2+}$, Ru(DIP)$_3^{3+}$, Ru(tpy)(bpy)O^{2+} {phen = 1,10-phenanthroline, DIP = tris(4,7-diphenyl-1,10-phenanthroline), tpy = 2,2′,2″-terpyridine, bpy = 2,2′-bipyridine}, and related structures were found helpful in recognition of structures in ribozymes, viral RNAs, rRNAs, and mRNAs with potential functional significance.[20] Recent studies have shown that noncoding RNAs play a key role in the regulation of cellular apoptosis, activation, and regeneration in the progression of liver cancer.[21]

Liver cancers are secondary or metastatic in nature, which is a more aggressive form of cancer where the cells are invaded from other parts of the body which is the primary origin of cancer.[22] Unfortunately, primary liver cancers remain undetected most of the time. Among the available treatment options, namely, invasive methods such as liver resection, radiation therapies, and chemotherapy, targeted chemotherapies are practiced. However, targeted chemotherapy is crucial for the longevity of patients with chronic liver cancers as it is more precise and selective towards the cancerous cells, leaving the normal cells unaffected. Literature reports demonstrate that targeted therapeutic drugs are capable of blocking the proteins to stop or slow down the growth or spread of cancer cells.[23]

In pursuit of designing RNA-targeted chemotherapeutic metallodrugs, herein, we describe two fully characterized new antitumor organometallics, namely, organotin(IV) and organoruthenium(II) complexes, their computational density functional theory (DFT) studies, and validation of their antitumor activity. The complexes exhibited selective recognition toward tRNA than DNA and impressive cytotoxic activity selectively against Huh7 (liver cancer cells) while they were nontoxic on the normal prostate cell line (PNT 2). Furthermore, the tRNA-targeted diphenytin(IV) drug candidate was found to be a potent antitumor agent for the liver cancer (Huh7) cell line, proven for the management of toxicity. This is the first report on the RNA-targeted organotin compound to the best of our knowledge.

RESULTS AND DISCUSSION

Synthesis of Drug Candidates. The ligand (HL) was formulated by the slight modification of Shit et al.[24] employing 1:1 condensation of 2-amino-2-methyl-1,3-propanediol with salicylaldehyde under reflux conditions. The corresponding drug candidates **1** and **2** were synthesized by in situ reaction of the methanolic solutions of the ligand (HL) and diphenyltin dichloride and [$RuCl_2$(*p*-cymene)]$_2$, respectively, as depicted in Scheme 1.

The products were air-stable and soluble in organic solvents such as methanol, dimethylsulfoxide (DMSO), and DMF (dimethyl formamide). Both **1** and **2** were thoroughly characterized by various spectroscopic tools [Fourier-transform

Scheme 1. Scheme for the Synthesis of 1 and 2

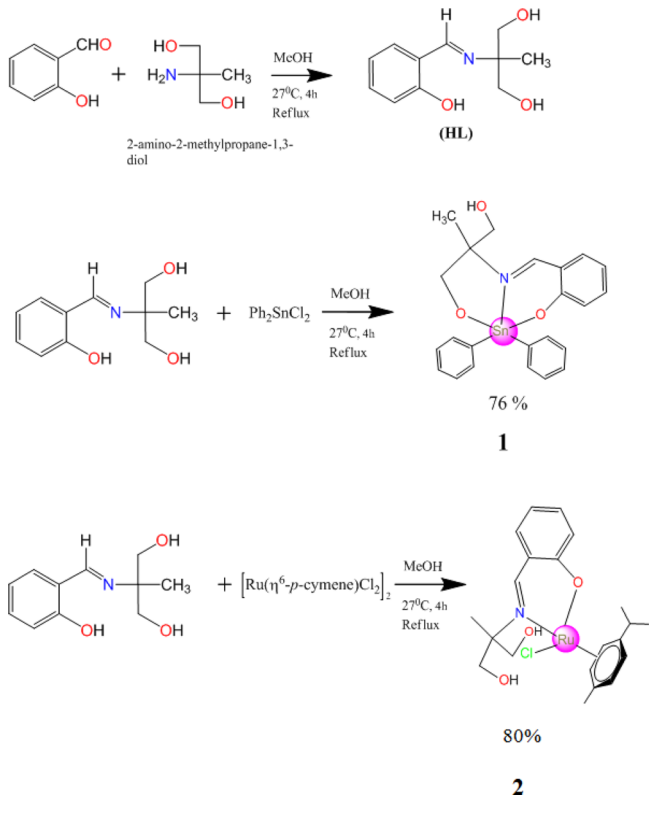

https://dx.doi.org/10.1021/acsomega.0c01206
ACS Omega 2020, 5, 15218−15228

infrared spectroscopy (FT-IR), UV−vis, and ^{1}H NMR/^{13}C NMR] and elemental analysis. The chemical structure of **1** was determined by single-crystal X-ray diffraction studies.

Single X-ray Crystal Description. Suitable crystals of **1** were acquired from the mother liquor through slow evaporation at room temperature after a few days. The single X-ray crystallographic studies revealed that **1** crystallized in the triclinic with the $P\bar{1}$ space group with $Z = 2$. A distorted square pyramidal geometry was formed by the Sn(IV) atom through the coordinating nitrogen and oxygen atoms from the tridentate Schiff base and carbon atoms of two phenyl groups (Figure 1a).

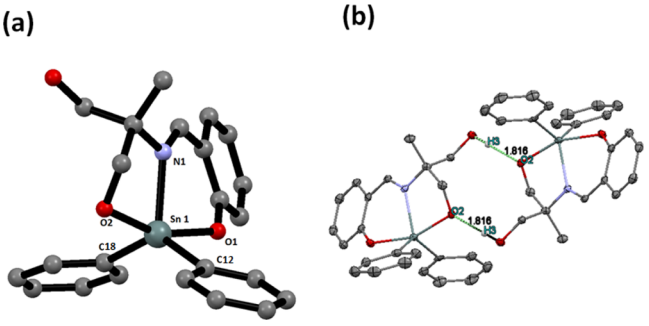

Figure 1. (a) ORTEP diagram of **1** labeled with the selected atoms. The hydrogen atoms have been dropped for clarity. (b) Crystal structure of **1** showing intermolecular hydrogen bonding.

The bond angles, bond distances, and experimental details have been shown in Tables 1, S1, and 2. The bond length (Sn−O1 = 2.1028 Å) was found to be larger in comparison to Sn−O2 (2.0761 Å) and the bond angle (O1−Sn−O2) was found to be 158.92°. These parameters are comparable to the previously reported complexes of diphenyltin dichloride exhibiting similar {Sn−O = 2.067−2.081 Å, O1−Sn−O2 = 155.4−161.6°} values.[12] The trigonality index, $\tau = (\beta - \alpha)/60$ [where β = O1−Sn1−O2 = 158.92(7)° and α = C12−Sn1−C18 = 133.74(10)°] was found to be 0.42 for **1**. On the basis of the τ value, the geometry around the Sn(IV) center in **1** could be described as distorted square pyramidal.[25] The crystal structure involves intermolecular hydrogen bonding interactions between unidentate oxygen atom (O2) and the hydrogen atom (H3) of the free −OH group such that O2−H3···O = 1.816 Å (Figure 1b).

Table 1. Selected Bond Lengths for 1

bond lengths	A^0	bond lengths	A^0
Sn1−O2	2.0844(17)	Sn1−C18	2.125(3)
Sn1−N1	2.180(2)	Sn1−C12	2.128(3)
Sn1−O1	2.1021(17)		

Table 2. Selected Bond Angles for 1

bond angles	deg	bond angles	deg
C18−Sn1−O2	95.02(9)	N1−Sn1−O2	76.62(7)
N1−Sn1−C18	110.65(9)	C12−Sn1−O2	94.87(9)
C12−Sn1−C18	133.74(10)	C12−Sn1−N1	115.61(9)
O1−Sn1−O2	159.07(7)	O1−Sn1−C18	94.56(9)
O1−Sn1−N1	82.59(7)	O1−Sn1−C12	91.87(9)

Spectroscopic Characterization. The FT-IR spectra of drug candidates **1** and **2** were recorded in the region of 4000−400 cm^{-1}. The azomethine stretching frequency of the ligand (HL) observed at 1630.06 cm^{-1} was lowered by 16 and 27 cm^{-1} upon complexation with metal ions in **1** and **2**, respectively, and found at 1613.3 and 1602.9 cm^{-1}, respectively. Bands at 3330.5 and 3401.1 cm^{-1} in **1** and **2** may be assigned to the aliphatic −OH group present in **1** and **2**, respectively.[26] The metal coordination was also substantiated by the vibrations at 525 and 446 cm^{-1} corresponding to Sn−O and Sn−N in **1**, respectively.[27] In complex **2**, the metal coordination bands were observed at 470, 548, and 438 cm^{-1} attributed to Ru−O, Ru−N, and Ru−Cl, respectively[28] (Figure S1).

^{1}H NMR spectra of **1** and **2** displayed the characteristic azomethine proton shift (−HC═N) at 9.88 and 8.70 ppm, respectively. The resonance signals at 3.41−3.44 ppm correspond to −CH_2 groups (aliphatic protons) while in drug candidate **2** these were found in the range of 3.82−3.88 ppm. Moreover, multiple peaks in the region 3.70−3.79 ppm were attributed to the aliphatic −OH group in **1**. In drug candidate **2**, it was found in the region 3.64−3.72 ppm. The aromatic regions in **1** and **2** were authenticated by the chemical shifts at 7.87−6.70 and 7.32−7.72 ppm, respectively. Singlets at 1.5 and 1.10 ppm were attributed to methyl protons in **1** and **2**, respectively (Figure S2). The isopropyl methyl protons in *p*-cymene resonated at 1.19−1.34 ppm. The chemical shift values for *p*-cymene aromatic protons were observed in the region 5.77−5.83 ppm[29] (Figure S3).

^{13}C{^{1}H} NMR spectra of **1** and **2** showed azomethine (−HC═N) and O−C═ group signatures at 170.04 and 163.96 and 170 and 150 ppm, respectively. The aromatic region was

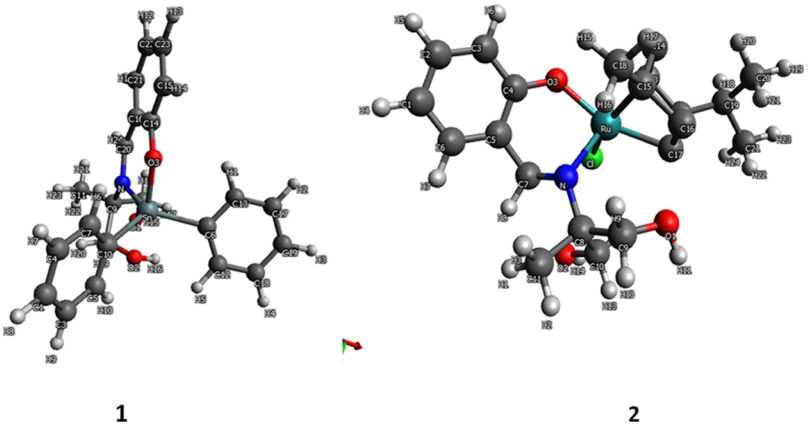

Figure 2. B3LYP/DFT-optimized structures of drug candidates **1** and **2**.

https://dx.doi.org/10.1021/acsomega.0c01206
ACS Omega 2020, 5, 15218−15228

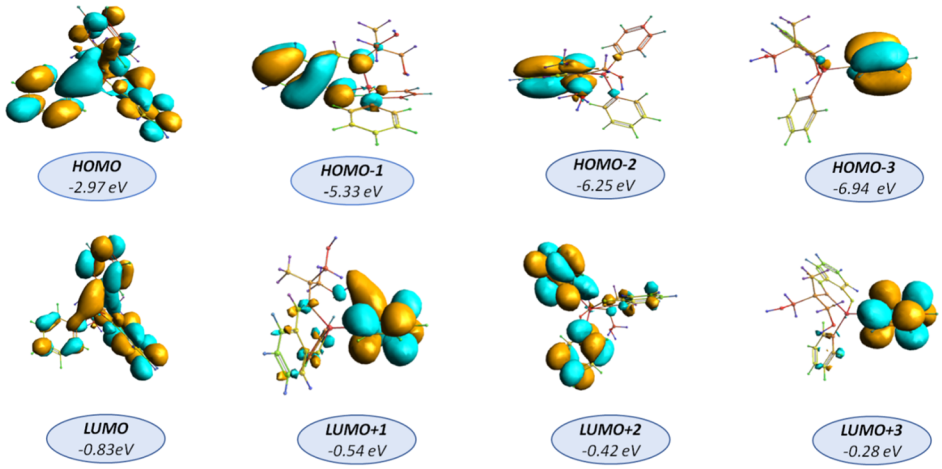

Figure 3. Frontier MOs contour plots of **1** using the B3LYP/DFT method.

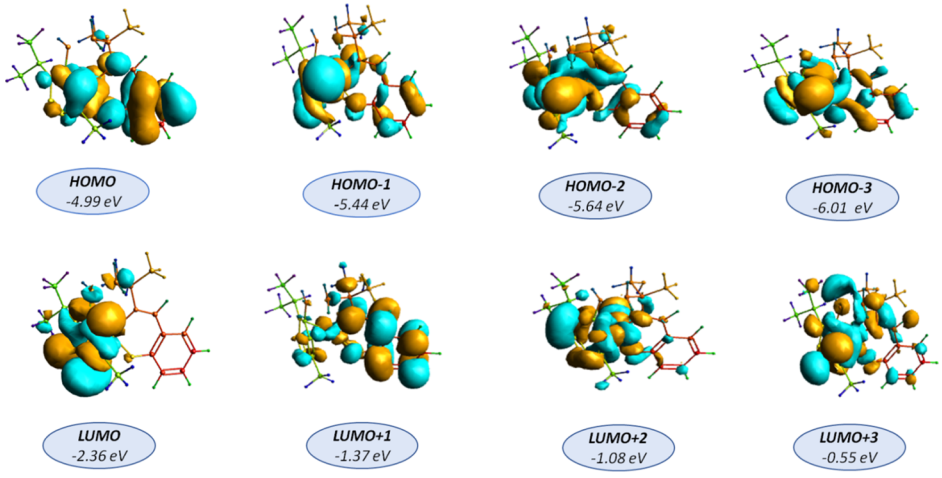

Figure 4. Frontier MOs contour plots of **2** using the B3LYP/DFT method.

described in the range 137.13−116.72 ppm in **1**.[26] The satellites with Sn were found in the region 133.89−122.69 ppm. In drug candidate **2**, the aromatic carbon atoms were marked in the region 132.3−115.85 ppm. The carbon atom adjacent to −OH and $-CH_3$ observed a chemical shift at 65.15 and 82.0 and 65.8 and 40.64 ppm, respectively. The appearance of resonance signals at 18.69, 23.5, and 30.5 ppm in drug candidate **2** were observed for $(CH_3)_{(HL)}$, $(CH_3)_{cym}$, and $(CH)_{cym}$, respectively. The resonance signals at 78.50 and 80.1 ppm were attributed to aromatic carbons of the *p*-cymene moiety, that is, for (C3/C5)cym and (C2/C6)cym[19] (Figures S5 and S6).

The ^{119}Sn NMR spectrum displayed a resonance signal at 223.7 ppm, which confirmed the five coordinated geometry around the Sn(IV) atom[30] (Figure S4).

The absorption spectra of **1** were obtained in DMSO at room temperature, which revealed bands at 278, 324, and 378 nm, consistent with intraligand (IL) transitions of the ligand.[31] The UV−vis spectra of **2** revealed absorption maxima at 340 nm and 268 nm, attributed to n−π^* and IL $\pi-\pi^*$ transition. The broad d−d band was observed at 432 nm in the visible part of the spectra[29] (Figure S8).

B3LYP/DFT Computational Studies. The gas phase structure optimization of **1** and **2** were carried out at the B3LYP/DFT level and optimized bond lengths and angles are tabulated in Tables S2−S4. The optimized structures of **1** and **2** at the ground state are represented in Figure 2. The optimized geometrical parameters were found in rational agreement with the spectroscopic results. In addition, the vibrational spectra were also reproduced to validate the proposed structure of **2** (Figure S7). The characteristic azomethine [ν(C═N)] and aliphatic [ν(−OH)] frequencies were found at 1605 and 3404 cm^{-1}, respectively, in the simulated IR spectra. The experimental FT-IR spectra consist of both harmonic and anharmonic vibrations while simulated vibrational spectra represented only harmonic vibrations. As a result, experimental values differ slightly from the calculated ones.[32] However, the characteristic vibrations were found quite similar in both the spectra, which validated the proposed structure of **2**.

In the gas phase, the molecular structure of **1** revealed that the Sn(IV) atom was coordinated to two carbon atoms from diphenyltin moieties in one plane and two oxygen atoms and one nitrogen atom from the Schiff base (HL) in the other plane, forming a distorted square pyramidal geometry around the Sn atom. The gas phase structure of **2** delineated that the Ru(II) atom was surrounded by carbon atoms from the *p*-cymene arene unit and one Cl atom and bidentate O/N atom from the Schiff base (HL) consisting of a "piano-stool" geometry around the Ru(II) atom.

The frontier molecular orbitals of **1** and **2** are shown in Figures 3 and 4. In drug candidates **1** and **2**, five highest occupied

https://dx.doi.org/10.1021/acsomega.0c01206
ACS Omega 2020, 5, 15218−15228

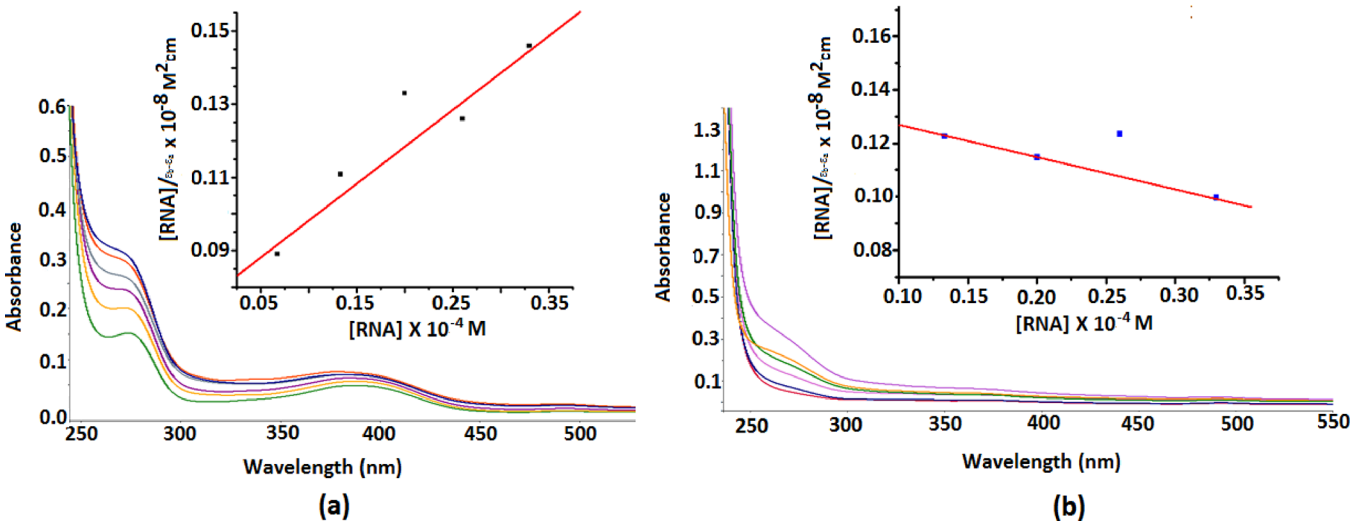

Figure 5. Absorption spectra of (a) **1** and (b) **2** with the concomitant addition of tRNA aliquots.

molecular orbitals (HOMOs) (HOMO to HOMO − 4) and five lowest unoccupied molecular orbitals (LUMOs) (LUMO to LUMO − 4) were observed. In drug candidate **1**, the HOMO and LUMO were distributed on the whole π-moiety in the ligand (HL) and the aromatic moiety of diphenyl rings and spread more on the metal ion. HOMO − 1 and HOMO − 2 almost consist of atomic orbitals of the aromatic moiety of the ligand (HL) and a very small amount on the metal ion, while HOMO − 3 consists of one phenyl ring and HOMO − 4 consists of both the phenyl rings in complex **1**. LUMO + 1 and LUMO + 2 dominated over one and both phenyl rings along with a small amount on the other aromatic rings in the complex as well as on the metal ion, respectively. LUMO + 3 spread more to one phenyl ring, and a very small amount was distributed on the other phenyl ring.

In drug candidate **2**, HOMO was distributed on the *p*-cymene ring as well as the whole π-moiety in the ligand (HL) and a significant amount of electronic density was present on the Ru(II) ion. HOMO − 1 to HOMO − 3 mostly incorporate atomic orbitals of the *p*-cymene ring and a significant amount from the π-moiety in the ligand as well as from the Ru(II) atom. The LUMO spread over the *p*-cymene ring as well as on the Ru(II) ion. LUMO + 1 was mostly distributed over the π-moiety in the ligand (HL) and a significant amount on the *p*-cymene ring and a small amount on nitrogen and oxygen coordinated to the metal ion. LUMO + 2 and LUMO + 3 were mainly made up of atomic orbitals of *p*-cymene rings and of the metal ion. A significant amount of contribution came from nitrogen and oxygen coordinated to the metal ion and from the chlorine atom attached to the metal ion.

Stability Studies in DMSO and Proteins. The stabilities of the drug candidates **1** and **2** were tested in DMSO as well as in proteins such as bovine serum albumin (BSA) by absorption spectroscopy. UV−visible absorption spectra of both the drug candidates **1** and **2** were recorded in DMSO at distinct time intervals (0, 1, 12, and 24 h). No appreciable change in either the intensity or the position of the absorption bands was observed in the course of time. Furthermore, absorption spectra revealed no significant changes, considerably after a duration of 24 h. The results implicated that their geometries do not change in solutions (Figure S8).

The stabilities of **1** and **2** in the presence of proteins such as BSA were also investigated spectrophotometrically. The interaction with BSA stabilizes the absorption bands for both the drug candidates **1** and **2**. Modest and progressive spectral changes were also noticed at the protein absorption band (279 nm) (Figure S9). In general, these findings suggested that BSA forms relatively stable adducts with the drug candidates and restricts their transformation and degradation.[33]

Interaction Studies with tRNA. RNAs represent a diverse and largely untapped class of biomolecules that can be exploited for designing efficient chemotherapeutic agents. An investigation of the molecular mechanism of the drug interaction with biomolecules, namely, RNAs, is of paramount importance as lnc RNAs are the prerequisite drug targets for the rational design of chemotherapeutic agents. Small molecules that specifically interact with unique RNA sites can regulate cell functions and are probably of great therapeutic potential.[34] Recently, it was found that Schiff base complexes interact with RNA through intercalation, which is evidenced by a characteristic "hypochromic" effect.[35] Nevertheless, there are fewer reports describing the binding profile of Schiff base complexes with tRNA.

In these experiments, the binding propensity of **1** and **2** with tRNA was examined using absorption spectroscopy. At varying concentrations of tRNA (0 to 5 × 10^{-5} M) to the stable concentration of **1** and **2** (0.067 × 10^{-5} M), a hyperchromic effect was observed at an IL band at 278 nm with a hyperchromism of 48 and 38%, respectively (Figure 5). By the observed "hyperchromic" trend, it can be elucidated that drug candidates **1** and **2** interact with tRNA through electrostatic mode. In our hypothesis, we suggest that aromatic moieties of diphenyltin in **1** and alkyl groups of *p*-cymene in **2** make a hydrophobic interaction with surfaces of RNA, the deep and the shallow grooves, most likely in the deep groove of RNA that are equivalent to the major groove of DNA lined by negatively charged phosphate groups. Additionally, the binding interactions can be stabilized by hydrogen bonding interactions between oxygen atoms of free −OH in **1** and **2** with RNA bases.

The binding strengths of **1** and **2** with the tRNA were quantified in terms of the intrinsic binding constant, K_b values, calculated using the Wolfe−Shimer equation.[36] K_b values were

https://dx.doi.org/10.1021/acsomega.0c01206
ACS Omega 2020, 5, 15218−15228

found to be 2.5 (±0.08) × 10^5 and 8.2 (±0.04) × 10^4 M^{-1} for **1** and **2**, respectively.

The comparative binding profiles for **1** and **2** with ctDNA were also studied; the results suggested a higher order of binding constants with tRNA as compared to ctDNA (K_b = 2.00 (±0.05) × 10^4 M^{-1} and 1.2 (±0.05) × 10^4 M^{-1}) (Figure S10). The justification for their specific RNA recognition could be (i) the highly exposed base pairs of RNA, which are easily accessed by the drug candidates and (ii) the bulge region of tRNA (which is not present in ctDNA), that provided greater overlap in RNA and enhanced the binding affinity of **1** and **2** with tRNA.[37]

The interaction of drug candidates with tRNA was further substantiated by the quite sensitive fluorescence spectroscopic technique. The drug candidates **1** and **2** demonstrated significant fluorescence at *ca.* 340 nm (λ_{em}) at an excitation wavelength of 260 nm (λ_{ex}), and a sequential increase in the fluorescence intensity was observed with no discernible shift upon addition of increasing aliquots of tRNA (0 to 4.00 × 10^{-5} M) (Figure S11). This phenomenon can be explained in terms of penetration of **1** and **2** into the hydrophobic environment of interior tRNA helices and was quite similar to that described in earlier research reports deciphering the binding profile of small molecules with RNAs.[38] The binding constant (K) values of **1** and **2** were obtained from the Scatchard equation[39] and found to be 4.3 (±0.02) × 10^5 and 1.62 (±0.02) × 10^5 M^{-1} for **1** and **2**, respectively.

Steady-state emission quenching experiments using ethidium bromide (EB) as a quencher supported the electrostatic interaction of drug candidates with tRNA. Upon addition of **1** and **2** to an EB−tRNA system such that [drug candidates **1**/**2**]/[tRNA] = 1:1 to 4:1, a significant quenching of the band at 600 nm was observed. These experimental results demonstrate that **1** and **2** displaced EB from the EB-tRNA system less efficiently as compared to classical intercalators[40] (Figure S12), ruling out their interaction through intercalative mode and confirming the electrostatic interaction of **1** and **2** with tRNA.

Quenching ability represented by the Stern−Volmer constant (K_{sv}) can be calculated by the equation

$$I_0/I = 1 + K_{sv}\cdot r$$

where I_0 and I denote the emission intensities in the presence and absence of **1** and **2**, K_{sv} represent the Stern−Volmer constant, and r denote the concentration ratio of **1** and **2** to tRNA. K_{sv} values were calculated as the slope of I_0/I versus r and were found to be 1.68 and 1.0 for drug candidates **1** and **2**, respectively.

Circular dichroism (CD), an efficient and powerful optical technique, was used to analyze the conformational changes upon interaction of **1** and **2** with tRNA. The CD spectrum of tRNA at 35 °C depicted two characteristic positive bands at 225 and 270 nm and two negative bands at 210 and 230 nm, in accordance with the double-stranded A-conformation.[38] On incubation of **1** and **2** to tRNA, the intensity of the negative band at 230 nm got reduced and an enhancement in the ellipticity of other bands at 210, 225, and 270 nm with a shift in corresponding wavelengths was observed (Figure 6). The observed shift can be explained in terms of conformational changes that occur in the tRNA molecule as a result of disruption of the base stacking interactions.

Cyclic voltammetry (CV) was further employed for the evaluation of mode of action and binding strength of the drug−RNA interaction. The electrochemical profile of binding of **1** and **2** with tRNA was studied in DMSO solution at room

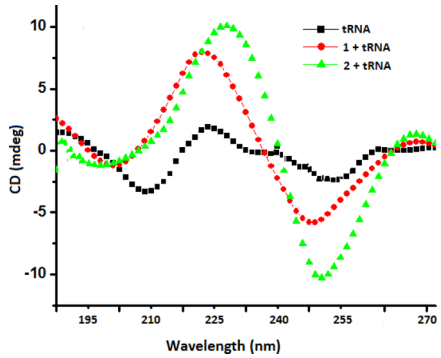

Figure 6. Overlay of CD spectra in tris HCl buffer at 35 °C. Concentration of [drug candidates **1**/**2**], [tRNA] = 1 × 10^{-4} M.

temperature at a scan rate of 0.2 V s^{-1} in the potential range of −1 to 1 V. The peak potential as well as the peak current of the drug candidates altered on interaction with tRNA. The cyclic voltammogram of **1** exhibited a quasireversible two-electron redox process[41] involving the Sn(IV)/Sn(II) couple with an anodic wave at E_{pa} = −0.25 V followed by a cathodic peak at E_{pc} = −0.63 V. For this couple, the difference in the cathodic and anodic peak potential ΔE_p and the ratio of the cathodic to anodic peak currents I_{pa}/I_{pc} were 0.38 V and 0.76, respectively. On the other hand, the CV of **2** featured a reduction of the Ru(II)/Ru(I) form at a cathodic peak potential of E_{pc} = −0.60 V. Reoxidation of the drug candidate was observed at E_{pa} = −0.28 V. The change in the peak potentials and the I_{pa}/I_{pc} ratio was found to be ΔE_p = 0.32 V, I_{pa}/I_{pc} = 0.90 which resulted in a quasireversible redox process.

The drug candidates experienced no new redox peaks with the addition of tRNA, but a substantial shift in the current was observed. In case of **1**, the change in the peak potentials (ΔE_p) and the ratio of the cathodic to anodic peak currents (I_{pa}/I_{pc}) were found to be 0.35 V and 0.88, respectively, while **2** observed a shift of 0.36 V in the peak potential and the current ratio was found to be 0.87 with tRNA (Figure 7).

Upon interaction of **1** and **2** with ctDNA, the shift in potentials (ΔE_p) of **1** and **2** was found to be 0.34 V and the current ratio (I_{pa}/I_{pc}) for **1** and **2** were found to be 0.84 and 0.81, respectively (Figure S13).

The observed result suggested that the shifts observed in the ΔE_p and I_{pa}/I_{pc} values were greater for both **1** and **2** with tRNA in comparison to ctDNA, indicating the preferential selectivity of both the drug candidates **1** and **2** with tRNA (Figure S14).

In Silico Studies of Drug−tRNA Interactions. To corroborate spectroscopic results of **1** and **2**, molecular docking technique was employed to reveal the most specific binding region in tRNA. The drug candidates **1** and **2** as flexible molecules were docked on tRNA as a rigid molecule. Docked conformations were investigated by the energy and hydrophobic interaction of the drug candidates with tRNA (PDB ID = 6TNA). The docking results implicated that **1** fit snugly into the active pocket of the anticodon arm in close proximity of C-27, C-28, A-29, A-31, A-38, G-30, U-41, and C-28 stabilized by hydrogen bonding (Figure 8). The docked pose model of **1** makes intermolecular H-bonds between the O atoms of free −OH in **1** (H-bonding acceptor group) and the H (H-bonding donor group) atom of RNA bases. Additionally, hydrophobic interactions are considered to be the main driving force in the strong binding of **1** to tRNA. On the other hand, drug candidate

https://dx.doi.org/10.1021/acsomega.0c01206
ACS Omega 2020, 5, 15218−15228

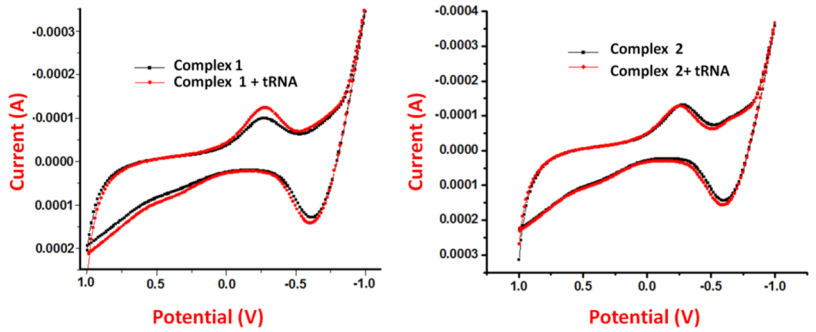

Figure 7. Cyclic voltammogram (1:2; DMSO/buffer solution) of **1** and **2**.

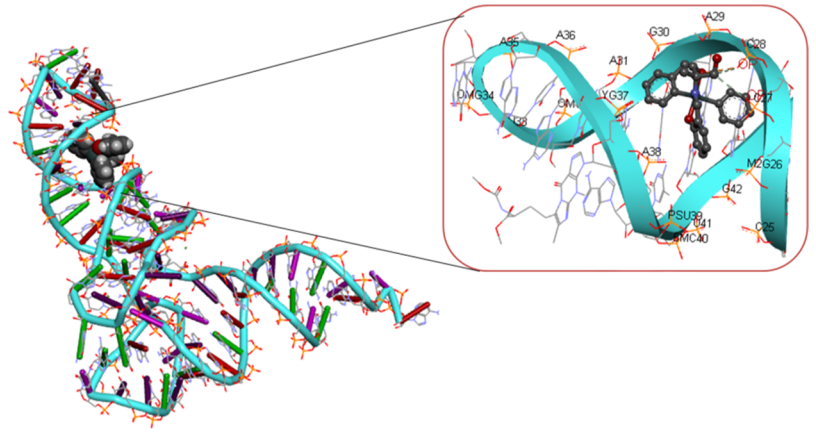

Figure 8. Best docked pose of **1** with the possible hydrogen bonding interactions. Hydrogen atoms have been erased for clarity.

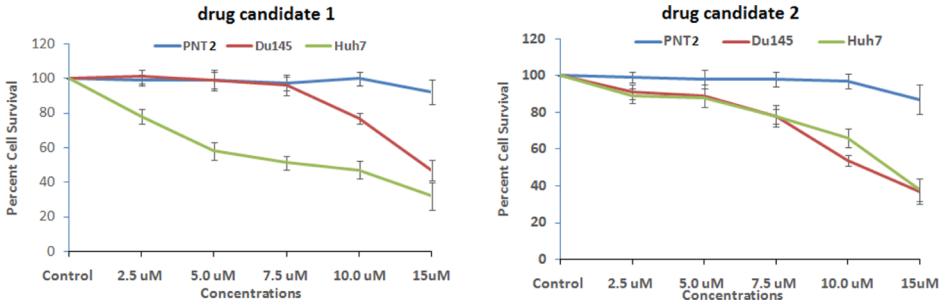

Figure 9. Survival of tumor cells as a function of different concentrations of **1** and **2** determined by the MTT test, after 48 h of incubation.

2 was inserted in the region ψ arm (Figure S15) in close proximity of U-54, U-50, C-49, P-55, and C-60.

The binding energies for the best docked pose of **1** and **2** with tRNA were quantified as −209.69 and −101.99 kJ mol^{-1}, respectively. The more negative binding energy value of **1** signified the greater binding propensity with tRNA, found in line with the results of other spectroscopic studies.

Cytotoxic Potential via MTT Assay. To determine the inhibitory effect of **1** and **2** on liver cancer cells (Huh-7) and prostate cancer cells (Du145), the effect of drug candidates **1** and **2** on the cell viability of Huh7 liver cancer cells and Du145 cells was assessed using 3-[4,5-dimethylthiazol-2-yl]-2,5-diphenyl tetrazoliumbromide (MTT) assay. The treatment of **1** and **2** (2.5−15 μM) after 48 h manifested dose-dependent growth inhibition of all these strains (Figure 9). The drug candidate **1** revealed the highest effect on the growth inhibition with an LC_{50} value of 8.0 and 12.6 μM for Huh7 and Du145, respectively, while for drug candidate **2**, LC_{50} values were found to be 12.5 and 11 μM for these two cancer cell lines, respectively. The LC_{50} values were found to be 14.9, 80.5, and 16 μM against Huh7, Du145, and the normal prostate epithelial PNT 2 cells with the standard drug cisplatin. The experimental data validated that both drug candidates **1** and **2** were capable of inhibiting the growth of drug-resistant cells, irrespective of the origin of the cells. Interestingly, no remarkable cell death was observed in the normal PNT2 cell lines upon treatment with **1** and **2**. Moreover, drug candidate **1** revealed good activity toward the liver cancer cell line (Huh7).

In conclusion, a positive correlation in the cytotoxic evaluation and binding affinity of **1** and **2** was experienced and resulted in the inhibition of tested cancer strains, followed by cell death with the treatment of an exceptionally low micromolar concentration of **1**. Devi and Yadav recently reported that among nonplatinum metallodrugs, organotin complexes have demonstrated safe administration, specific targeted drug uptake by the cancerous cell line, and promising activity in pharmaceutical chemistry.[42]

https://dx.doi.org/10.1021/acsomega.0c01206
ACS Omega 2020, 5, 15218−15228

CONCLUSIONS

Organometallic complexes of tin and ruthenium are enjoying resurgence among nonplatinum antitumor chemotherapeutic metallodrugs owing to their mechanism of action, targeting macromolecular synthesis, mitochondrial energy metabolism, and ultimately nucleic acids. In lieu of this, two organometallic antitumor drug candidates were prepared and characterized by using various spectroscopic and analytical techniques. Single X-ray crystallographic studies revealed that **1** formed a distorted square pyramidal geometry around Sn(IV) with two phenyl groups and the imino-N1 atom occupying the equatorial positions, while the axial positions were occupied by a phenoxide-O1 and a unidentate O2 atom. The geometry optimization of **1** and **2** was carried out by B3LYP/DFT studies. In vitro tRNA binding profiles of **1** and **2** were assessed using biophysical methods. The aromatic moieties of diphenyltin in **1** and alkyl groups of *p*-cymene in **2** make hydrophobic interactions with RNA surfaces. In addition, the binding interactions were stabilized by hydrogen bonding interactions between oxygen atoms of free −OH in **1** and **2** with RNA bases. Cytotoxic evaluation of **1** and **2** against two cancer cell lines Huh7 (liver cancer cells) and Du145 (prostate) and one normal prostate cell line (PNT 2) was carried out by MTT assay, which revealed a good selective activity of **1** toward the liver cancer cell line (Huh7). However, both the drug candidates were screened as nontoxic toward normal prostate epithelial PNT 2 cells. The corroborative results demonstrated that both the drug candidates **1** and **2** can act as promising antitumor agents and warrant further biological investigation.

EXPERIMENTAL SECTION

Materials and Instrumentation. Salicylaldehyde, 2-amino-2-methyl-1,3-propanediol from Sigma-Aldrich, KOH, diphenyltin dichloride, and dichloro(*p*-cymene)ruthenium(II) dimer (Alfa Aesar) were purchased and used as received. Solvents used were of purity grade. Infrared spectra were recorded (KBr disk, 400−4000 cm^{-1}) on a PerkinElmer model 1320 spectrometer. Elemental analysis was performed on a Carlo Erba Analyser model 1106. NMR analysis of **1** and **2** was carried out on a Bruker DRX-400 spectrometer with Me_2SO-d_6 as the solvent. Absorption spectra were recorded on a PerkinElmer Lambda 25 spectrophotometer using cuvettes of 1 cm path length, and the data were reported in λ_{max}/nm. The disodium salt of tRNA (type IX) from Torula yeast was purchased from Sigma Chemicals Co. and stored at 4 °C. RNA solution was prepared in 10 mM Tris−HCl buffer (pH 7.3) and stored at 8 °C for 24 h. To ensure the homogeneity of solution, it was stirred at frequent intervals.

To study the stability of drug candidates in DMSO as well as in proteins, electronic spectra of the drug candidates were taken before and after the addition of BSA at a stoichiometric ratio of 3:10 (metal to protein) for 24 h at room temperature in 10 mM Tris−HCl buffer (pH = 7.3).

The interaction studies of the drug candidates with tRNA were performed in Tris−HCl buffer (pH = 7.3). The concentration per base pairs for RNA was measured spectrophotometrically at 260 nm assuming ε = 7700 M^{-1} cm^{-1}. Fluorescence studies were performed on a Shimadzu RF-5301PC spectrofluorophotometer. CD spectra were obtained on a Jasco J-815-CD spectropolarimeter at room temperature. The electrochemical profile was studied on a CH instrument electrochemical analyzer. High-purity H_2O and DMSO (95:5) were used for CV studies with 0.4 M KNO_3 as a supporting electrolyte. A three-electrode configuration was employed consisting of a Pt disk as the working electrode, a Pt wire as the counter electrode, and Ag/AgCl as the reference electrode. All the measurements were made under the N_2 atmosphere.

Computational DFT Studies. Complete geometry optimization was ascertained using DFT methods with the hybrid B3LYP functional. The optimized structure was further recalculated using a def2-TZVP basis set for all atoms to calculate the HOMO and LUMO energies. To accelerate the calculations, the resolution of identity approximation was employed with the decontracted auxiliary def2-SVP/J and def2-TZV/J Coulomb fitting basis sets and the chain-of-spheres (RIJCOSX) approximation to exact exchange as instigated in ORCA.[43−45]

Synthesis of Ph_2Sn(HL), 1. The Schiff base (HL) was prepared by refluxing methanolic solution of 2-amino-2-methyl-1,3-propanediol (5.0 mmol) with salicylaldehyde (5.0 mmol). After 4 h, a yellow clear solution was formed. The methanolic solution (20 mL) of diphenyltin dichloride (5 mmol) and yellow solution (5 mmol) of the ligand (HL) were mixed and refluxed for 4 h till the completion of the reaction. The resulting mixture was put aside at room temperature. Yellow crystals grew after a couple of days and were separated from the mother liquor and dried in air. **1** was air-stable and found soluble in solvents such as methanol, DMSO, and DMF. The structure of **1** was determined by single X-ray crystallographic studies and other spectroscopic techniques.

*Ph_2Sn(HL), **1***. Yield: 76%, mp 170 °C; CCDC: 1976012. Anal. Calcd for [$C_{23}H_{24}NO_3Sn$] (%): C, 58.21; H, 5.29; N, 2.83. Found: C, 57.38; H, 5.20; N, 2.67. UV−vis (1×10^{-4} M, DMSO, λ_{max} nm): 278 ($\pi-\pi^*$), 324 ($n-\pi^*$), 378. FT-IR (KBr pallet, ν_{max}/cm^{-1}):1613.3 ν(C═N), 3330.5 ν(R−OH), 446 ν(Sn−N), 525 ν(Sn−O). ^{1}H NMR (400 MHz, $CDCl_3$-d_6, δ, ppm): 1.50 (s, $-CH_3$) ppm, 3.41 (d, 2H, $-CH_2-$, J = 12 Hz), 3.70−3.79 (t, 1H, R−OH), 5.30 (s, 2H, $-Sn-O-CH_2-$), 6.72 (t, 1H, −CH, J = 8.0 Hz), 6.83 (t, 2H, −CH, J = 8.0 Hz), 6.96 (d, 1H, −CH, J = 8.0 Hz), 7.00 (t, −CH, J = 8.0 Hz), 7.15 (d, −CH, J = 8.0 Hz), 7.25 (d, −CH, J = 8.0 Hz), 7.34 (d, −CH, J = 8.0 Hz), 7.41 (m, −CH, J = 8.0 Hz), 7.53 (t, −CH, J = 8.0 Hz), 7.87 (m, −CH, J = 8.0 Hz), 9.88 (s, N═CH). ^{13}C{^{1}H} NMR (100 MHz, $CDCl_3$-d_6, δ, ppm): 170.04 (C-1), 163.96 (C-7), 137.13 (C-13), 136.88 (C-12), 136.70 (C-15), 119.93 (C-14), 118.16 (C-6), 117.77 (C-3), 117.69 (C-2), 117.47 (C-4), 116.72 (C-5), 18.81 (C-11), 64.29 (C-8), 65.15 (C-10), 82.0 (C-9). ^{119}Sn NMR (149.19 MHz, DMSO-d_6[6] ppm): −223.7.

*Synthesis of Ru(η^6-p-cymene)(HL)Cl, **2***. A similar method was opted for the preparation of drug candidate **2** as for **1** by using [$RuCl_2$(*p*-cymene)]$_2$ instead of diphenyltin dichloride. Slow evaporation of the reaction mixture yielded a brown precipitate after a few days at room temperature. The reaction mixture was dried in vacuum and extracted with dichloromethane, which was found to be soluble in methanol, DMSO, and DMF.

*Ru(η^6-p-cymene)(HL)Cl, **2***. Yield: 80%, mp 215 °C. Anal. Calcd for [$C_{21}H_{28}ClNO_3Ru$] (%): C, 52.66; H, 5.89; N, 2.92. Found: C, 51.28; H, 6.10; N, 2.83. UV−vis (1×10^{-4} M, DMSO, λ_{max} nm): 268 ($\pi-\pi^*$), 340 ($n-\pi^*$), 432 (d−d). FT-IR (KBr pallet, ν_{max}/cm^{-1}): 1602.9 ν(C═N), 3401.1 ν(R−OH), 548 ν(Ru−N), 470 ν(Ru−O), 438 ν(Ru−Cl). ^{1}H NMR (100 MHz, $CDCl_3$-d_6, δ, ppm): 1.10 (s, 3H, $-CH_3$) ppm, 1.34 (s, $-CH_3$, cym, 3H), 1.24 (d, CH_3, cym, 6H, J = 5.0 Hz), 2.52 (m, CH, cym, 1H), 3.68 (t, 1H, R−OH, J = 8.0 Hz), 3.82 (d, 2H, $-CH_2-$,

https://dx.doi.org/10.1021/acsomega.0c01206
ACS Omega 2020, 5, 15218−15228

J = 6.0 Hz), 7.34 (d, 1H, J = 2.0 Hz), 7.46 (t, 1H, J = 10.0 Hz), 7.56 (t, 1H, J = 6.0 Hz), 7.72 (d, 1H, J = 2.0 Hz), 5.82 (d, H3 and H5, 2H, J = 1.0 Hz), 5.77 (d, H2 and H6, 2H, J = 2.0 Hz). $^{13}C\{^1H\}$ NMR (100 MHz, δ, ppm): 170.0 (C-1), 150.0 (C-11), 30.5 (CH)cym, 78.50 (C3 and C5)cym, 80.1 (C2 and C6)cym, 23.5 (CH_3)cym, 18.69 (C-13), 132.3 (C-4), 130.26 (C-7), 127.79 (C-8), 120.68 (C-9), 118.02 (C-10).

Single X-ray Crystallographic Studies. A Bruker SMART APEX CCD diffractometer (100 K) was used to record crystallographic data for **1** excited with graphite monochromatic Mo Kα radiation (k = 0.71073 Å). The scattering factors for the atoms, linear absorption coefficients, and the anomalous dispersion corrections were taken from the International Tables for X-ray crystallography. The data were integrated and reduced with the help of SAINT software. Empirical absorption correction was adapted to the collected reflections with the SADABS program[46] and the space group was established using XPREP. The crystal structure was solved by direct methods with SHELXTL-97 and refined on F2 by full-matrix least-squares employing a SHELXTL-97 programme package.[47] The selected crystallographic details are shown in Table S1.

Computational Docking Studies. Computational docking studies were carried out employing HEX 8.0 software,[48] an interactive molecular graphics program to calculate and display feasible docking modes of nucleic acids as well as proteins. The Discovery Studio molecular graphics program was utilized to visualize the docked pose structures.

Cell Culture and Treatment. We selected two drug-resistant cells, Du145 (prostate) and Huh7 (liver), and one normal prostate epithelial cell, PNT2, for the study. PNT2 and Du145 cells were grown in RPMI 1640 (Invitrogen, Carlsbad, CA) supplemented with 10% FBS and 1% penicillin or streptomycin. Huh7 cells were cultured in DMEM supplemented with 10% FBS and 1% penicillin/streptomycin. Each strain was maintained under standard cell culture conditions at 37 °C and 5% CO_2 environment. The cells (60−70% confluent) were treated with the drug candidates **1** and **2** for 48 h in complete growth medium.

Cell Viability Assay. The effect of **1** and **2** on cell viability was assessed by MTT (Sigma, Mo) assay. Briefly, the cells were seeded in 96-well dishes at a density of 3.5×10^3 cells per well. The cells were allowed to attach for 24 h before incubation with fresh medium containing either **1** or **2** (2.5−15.0 μM) for 48 h. After incubation for 48 h at 37 °C, an MTT assay was performed as described previously.[49]

■ ASSOCIATED CONTENT

Supporting Information

The Supporting Information is available free of charge at https://pubs.acs.org/doi/10.1021/acsomega.0c01206.

Crystallographic details; B3LYP/DFT-optimized bond lengths/angles; FT-IR spectra, ^1H, ^{13}C, and ^{119}Sn NMR spectra; overlay of experimental and B3LYP/DFT-optimized FT-IR spectra of **2**; time course UV−vis spectra of **1** and **2** in DMSO and in the presence of BSA; binding curves of **1** and **2** with ctDNA/tRNA; CV spectra in the presence of ctDNA; and docked pose model of **2** with tRNA (PDF)

Crystallographic data of the drug candidates (CIF)

■ AUTHOR INFORMATION

Corresponding Author

Farukh Arjmand − *Department of Chemistry, Aligarh Muslim University, Aligarh 202002, India;* orcid.org/0000-0003-4677-2682; Email: farukh.arjmand18@gmail.com

Authors

Huzaifa Yasir Khan − *Department of Chemistry, Aligarh Muslim University, Aligarh 202002, India*

Santosh K. Maurya − *Section of Genetics, Department of Zoology, Aligarh Muslim University, Aligarh 202002, India*

Hifzur R. Siddique − *Section of Genetics, Department of Zoology, Aligarh Muslim University, Aligarh 202002, India*

Shariq Yousuf − *Department of Chemistry, Aligarh Muslim University, Aligarh 202002, India*

Complete contact information is available at: https://pubs.acs.org/10.1021/acsomega.0c01206

Notes

The authors declare no competing financial interest.

■ ACKNOWLEDGMENTS

The authors are thankful to the Instrumentation Centre, Department of Chemistry, Aligarh Muslim University, Aligarh, for spectroscopic analysis. H.Y.K. sincerely expresses his gratitude to the Department of Science and Technology, New Delhi, for providing a DST-INSPIRE Senior Research Fellowship (DST/AORC-IF/UPGRD/IF160130). The authors extend their appreciation to Dr. Musheer Ahmad, Department of Applied Chemistry, Aligarh Muslim University, Aligarh, for refining single X-ray crystal data **1** and extend thanks to IIT Kanpur for solving the structure.

■ REFERENCES

(1) Gielen, M. Review: Organotin compounds and their therapeutic potential: a report from the Organometallic Chemistry Department of the Free University of Brussels. *Appl. Organomet. Chem.* **2002**, *16*, 481−494.

(2) Alama, A.; Tasso, B.; Novelli, F.; Sparatore, F. Organometallic compounds in oncology: implications of novel organotins as antitumor agents. *Drug Discovery Today* **2009**, *14*, 500−508.

(3) Parveen, S.; Arjmand, F.; Tabassum, S. Development and future prospects of selective organometallic compounds as anticancer drug candidates exhibiting novel modes of action. *Eur. J. Med. Chem.* **2019**, *175*, 269−286.

(4) Koch, B.; Baul, T. S. B.; Chatterjee, A. Cell proliferation inhibition and antitumor activity of novel alkyl series of diorganotin (IV) compounds. *J. Appl. Toxicol.* **2008**, *28*, 430−438.

(5) Gupta, R. K.; Pandey, R.; Sharma, G.; Prasad, R.; Koch, B.; Srikrishna, S.; Li, P.-Z.; Xu, Q.; Pandey, D. S. DNA binding and anticancer activity of redox-active heteroleptic piano-stool Ru (II), Rh (III), and Ir (III) complexes containing 4-(2-methoxypyridyl) phenyldipyrromethene. *Inorg. Chem.* **2013**, *52*, 3687−3698.

(6) Zaki, M.; Hairat, S.; Aazam, E. S. Scope of organometallic compounds based on transition metal-arene systems as anticancer agents: starting from the classical paradigm to targeting multiple strategies. *RSC Adv.* **2019**, *9*, 3239−3278.

(7) Tabassum, S.; Pettinari, C. Chemical and biotechnological developments in organotin cancer chemotherapy. *J. Organomet. Chem.* **2006**, *691*, 1761−1766.

(8) Arjmand, F.; Parveen, S.; Tabassum, S.; Pettinari, C. Organo-tin antitumor compounds: Their present status in drug development and future perspectives. *Inorg. Chim. Acta* **2014**, *423*, 26−37.

(9) Hadjikakou, S.; Hadjiliadis, N. Antiproliferative and anti-tumor activity of organotin compounds. *Coord. Chem. Rev.* **2009**, *253*, 235−249.
(10) Khan, A.; Parveen, S.; Khalid, A.; Shafi, S. Recent advancements in the anticancer potentials of phenylorganotin (IV) complexes. *Inorg. Chim. Acta* **2020**, *505*, 119464.
(11) (a) Díaz-García, D.; Sommerova, L.; Martisova, A.; Skoupilova, H.; Prashar, S.; Vaculovic, T.; Kanicky, V.; del Hierro, I.; Hrstka, R.; Gómez-Ruiz, S. Mesoporous silica nanoparticles functionalized with a dialkoxide diorganotin(IV) compound: In search of more selective systems against cancer cells. *Microporous Mesoporous Mater.* **2020**, *300*, 110154. (b) Díaz-García, D.; Cenariu, D.; Pérez, Y.; Cruz, P.; del Hierro, I.; Prashar, S.; Fischer-Fodor, E.; Gómez-Ruiz, S. Modulation of the mechanism of apoptosis in cancer cell lines by treatment with silica-based nanostructured materials functionalized with different metallodrugs. *Dalton Trans.* **2018**, *47*, 12284−12299.
(12) Beltrán, H. I.; Damian-Zea, C.; Hernández-Ortega, S.; Nieto-Camacho, A.; Ramírez-Apan, M. T. Synthesis and characterization of di-phenyl-tinIV-salicyliden-ortho-aminophenols: Analysis of in vitro antitumor/antioxidant activities and molecular structures. *J. Inorg. Biochem.* **2007**, *101*, 1070−1085.
(13) Zeng, L.; Gupta, P.; Chen, Y.; Wang, E.; Ji, L.; Chao, H.; Chen, Z.-S. The development of anticancer ruthenium (II) complexes: from single molecule compounds to nanomaterials. *Chem. Soc. Rev.* **2017**, *46*, 5771−5804.
(14) (a) Pettinari, R.; Marchetti, F.; Condello, F.; Pettinari, C.; Lupidi, G.; Scopelliti, R.; Mukhopadhyay, S.; Riedel, T.; Dyson, P. J. Ruthenium (II)−arene RAPTA type complexes containing curcumin and bisdemethoxycurcumin display potent and selective anticancer activity. *Organometallics* **2014**, *33*, 3709−3715. (b) Allardyce, C. S.; Dyson, P. J.; Ellis, D. J.; Heath, S. L. [Ru(η^6-p-cymene)Cl_2(pta)](pta= 1, 3, 5-triaza-7-phosphatricyclo-[3.3.1.1] decane): a water soluble compound that exhibits pH dependent DNA binding providing selectivity for diseased cells. *Chem. Commun.* **2001**, *15*, 1396−1397.
(15) Adhireksan, Z.; Davey, G. E.; Campomanes, P.; Groessl, M.; Clavel, C. M.; Yu, H.; Nazarov, A. A.; Yeo, C. H.; Ang, W. H.; Dröge, P.; Rothlisberger, U.; Dyson, P. J.; Davey, C. A. Ligand substitutions between ruthenium−cymene compounds can control protein versus DNA targeting and anticancer activity. *Nat. Commun.* **2014**, *5*, 3462.
(16) Bratsos, I.; Jedner, S.; Gianferrara, T.; Alessio, E. Ruthenium anticancer compounds: challenges and expectations. *CHIMIA Int. J. Chem.* **2007**, *61*, 692−697. (b) Lentz, F.; Drescher, A.; Lindauer, A.; Henke, M.; Hilger, R. A.; Hartinger, C. G.; Scheulen, M. E.; Dittrich, C.; Keppler, B. K.; Jaehde, U. Pharmacokinetics of a novel anticancer ruthenium complex (KP1019, FFC14A) in a phase I dose-escalation study. *Anti-Cancer Drugs* **2009**, *20*, 97−103. (c) Gianferrara, T.; Bratsos, I.; Alessio, E. A categorization of metal anticancer compounds based on their mode of action. *Dalton Trans.* **2009**, 7588−7598.
(17) (a) Gasser, G.; Ott, I.; Metzler-Nolte, N. Organometallic Anticancer Compounds. *J. Med. Chem.* **2011**, *54*, 3−25. (b) Jakupec, M. A.; Galanski, M.; Arion, V. B.; Hartinger, C. G.; Keppler, B. K. Antitumour metal compounds: more than theme and variations. *Dalton Trans.* **2008**, *2*, 183−194. (c) Dyson, P. J.; Sava, G. Metal-based antitumour drugs in the post genomic era. *Dalton Trans.* **2006**, *16*, 1929−1933. (d) Clarke, M. J. Ruthenium metallopharmaceuticals. *Coord. Chem. Rev.* **2002**, *232*, 69−93. (e) Smith, G. S.; Therrien, B. Targeted and multifunctional arene ruthenium chemotherapeutics. *Dalton Trans.* **2011**, *40*, 10793−10800.
(18) Ginzinger, W.; Mühlgassner, G.; Arion, V. B.; Jakupec, M. A.; Roller, A.; Galanski, M.; Reithofer, M.; Berger, W.; Keppler, B. K. A SAR study of novel antiproliferative ruthenium and osmium complexes with quinoxalinone ligands in human cancer cell lines. *J. Med. Chem.* **2012**, *55*, 3398−3413.
(19) Yousuf, I.; Arjmand, F.; Tabassum, S.; Ahmad, M. Design and synthesis of a DNA intercalative half-sandwich organoruthenium (ii)−chromone complex: cytotoxicity evaluation and topoisomerase Iα inhibition assay. *New J. Chem.* **2019**, *43*, 5475−5487.
(20) Chow, C. S.; Bogdan, F. M. A structural basis for RNA−ligand interactions. *Chem. Rev.* **1997**, *97*, 1489−1514.
(21) O'Brien, A.; Zhou, T.; Tan, C.; Alpini, G.; Glaser, S. Role of Non-Coding RNAs in the Progression of Liver Cancer: Evidence from Experimental Models. *Cancers* **2019**, *11*, 1652.
(22) https://www.healthline.com/health/liver-metastases,17 /09/2018.
(23) https://www.cancer.net/navigating-cancer-care/how-cancer-treated/personalized-and-targeted-therapies/understanding-targeted-therapys, 05/2020.
(24) Shit, S.; Rosair, G.; Mitra, S. A new tetranuclear copper (II) Schiff base complex containing Cu_4O_4 cubane core: Structural and spectral characterizations. *J. Mol. Struct.* **2011**, *991*, 79−83.
(25) Shujah, S.; Zia-ur-Rehman, N.; Muhammad, N.; Shah, A.; Ali, S.; Meetsma, A.; Hussain, Z. Homobimetallic organotin (IV) complexes with hexadentate Schiff base: Synthesis, crystal structure and antimicrobial studies. *J. Organomet. Chem.* **2014**, *759*, 19−26.
(26) Ansari, I. A.; Sama, F.; Raizada, M.; Shahid, M.; Rajpoot, R. K.; Siddiqi, Z. A. Synthesis and spectral characterization of 2-((2-hydroxybenzylidene) amino)-2-methylpropane-1, 3-diol derived complexes: Molecular docking and antimicrobial studies. *J. Mol. Struct.* **2017**, *1127*, 479−488.
(27) Yin, H. D.; Hong, M.; Li, G.; Wang, D. Q. Synthesis, characterization and structural studies of diorganotin(IV) complexes with Schiff base ligand salicylaldehyde isonicotinylhydrazone. *J. Organomet. Chem.* **2005**, *690*, 3714−3719.
(28) Jia, W.-G.; Zhang, H.; Zhang, T.; Xie, D.; Ling, S.; Sheng, E.-H. Half-sandwich ruthenium complexes with Schiff-base ligands: Syntheses, characterization, and catalytic activities for the reduction of nitroarenes. *Organometallics* **2016**, *35*, 503−512.
(29) Haribabu, J.; Sabapathi, G.; Tamizh, M. M.; Balachandran, C.; Bhuvanesh, N. S. P.; Venuvanalingam, P.; Karvembu, R. Water-soluble mono-and binuclear Ru(η^6-p-cymene) complexes containing indole thiosemicarbazones: Synthesis, DFT modeling, biomolecular interactions, and in vitro anticancer activity through apoptosis. *Organometallics* **2018**, *37*, 1242−1257.
(30) Arjmand, F.; Sayeed, F.; Parveen, S. In vitro binding studies of organotin(IV) complexes of 1,2-bis(1H-benzimidazol-2-yl)ethane-1,2-diol with CT-DNA and nucleotides (5'-GMP and 5'-TMP): Effect of the ancillary ligand on the binding propensity. *J. Organomet. Chem.* **2011**, *696*, 3836−3845.
(31) Arjmand, F.; Muddassir, M.; Yousuf, I. Design and synthesis of enantiomeric (R)-and (S)-copper (II) and diorganotin (IV)-based antitumor agents: Their in vitro DNA binding profile, cleavage efficiency and cytotoxicity studies. *J. Photochem. Photobiol., B* **2014**, *136*, 62−71.
(32) Khan, R. A.; Usman, M.; Dhivya, R.; Balaji, P.; Alsalme, A.; AlLohedan, H.; Arjmand, F.; AlFarhan, K.; Akbarsha, M. A.; Marchetti, F.; Pettinari, C. Heteroleptic Copper (I) Complexes of "Scorpionate" Bis-pyrazolyl Carboxylate Ligand with Auxiliary Phosphine as Potential Anticancer Agents: An Insight into Cytotoxic Mode. *Sci. Rep.* **2017**, *7*, 45229.
(33) Tamasi, G.; Bernini, C.; Corbini, G.; Owens, N. F.; Messori, L.; Scaletti, F.; Massai, L.; Giudice, P. L.; Cini, R. Synthesis, spectroscopic and DFT structural characterization of two novel ruthenium(III) oxicam complexes. In vivo evaluation of anti-inflammatory and gastric damaging activities. *J. Inorg. Biochem.* **2014**, *134*, 25−35.
(34) Tor, Y. RNA and the small molecule World. *Angew. Chem.* **1999**, *111*, 1168−1685.
(35) Zehra, S.; Roisnel, T.; Arjmand, F. Enantiomeric Amino Acid Schiff Base Copper (II) Complexes as a New Class of RNA-Targeted Metallo-Intercalators: Single X-Ray Crystal Structural Details, Comparative in Vitro DNA/RNA Binding Profile, Cleavage, and Cytotoxicity. *ACS Omega* **2019**, *4*, 7691−7705.
(36) Wolfe, A.; Shimer, G. H., Jr.; Meehan, T. Polycyclic aromatic hydrocarbons physically intercalate into duplex regions of denatured DNA. *Biochemistry* **1987**, *26*, 6392−6396.
(37) Liang, X.-L.; Tan, L.-F. Nucleic Acid (Calf Thymus-DNA, Yeast tRNA) Binding and Cytotoxic Properties of a Dinuclear (Ru, Co) Metal Polypyridyl Complex. *Aust. J. Chem.* **2010**, *63*, 1453−1461.

https://dx.doi.org/10.1021/acsomega.0c01206
ACS Omega 2020, 5, 15218−15228

(38) (a) Khan, H. Y.; Tabassum, S.; Arjmand, F. Evaluation of cytotoxic potential of structurally well-characterized RNA targeted ionic non-steroidal anti-inflammatory (NSAID) Cu (II) & Zn (II) DACH−mefenamato drug conjugates against human cancer cell lines. *RSC Adv.* **2020**, *10*, 166−178. (b) Sharma, S.; Toupet, L.; Ahmad, M.; Arjmand, F. Synthesis, characterization, and crystal structure of RNA targeted L- and D-phenylalanine-(1,10-phen)−copper(II) conjugate complexes: comparative in vitro RNA binding profile of enantiomers and their biological evaluation by morphological studies andantibacterial activity. *RSC Adv.* **2016**, *6*, 79372−79382.

(39) Hearly, E. F. Quantitative Determination of DNA−Ligand Binding Using Fluorescence Spectroscopy. *J. Chem. Educ.* **2007**, *84*, 1304−1307.

(40) Luedtke, N. W.; Hwang, J. S.; Nava, E.; Gut, D.; Kol, M.; Tor, Y. The DNA and RNA specificity of eilatin Ru(II) complexes as compared to eilatin and ethidium bromide. *Nucleic Acids Res.* **2003**, *31*, 5732−5740.

(41) Arshad, N.; Farooqi, S. I. Cyclic Voltammetric DNA Binding Investigations on Some Anticancer Potential Metal Complexes: a Review. *Appl. Biochem. Biotechnol.* **2018**, *186*, 1090−1110.

(42) Devi, J.; Yadav, J. Recent Advancements in Organotin (IV) Complexes as Potential Anticancer Agents. *Anti-Cancer Agents Med. Chem.* **2018**, *18*, 335−353.

(43) Neese, F. The ORCA program system. *Wiley Interdiscip. Rev.: Comput. Mol. Sci.* **2012**, *2*, 73−78.

(44) Neese, F. O. R. C. A. *An Ab Initio: Density Functional and Semi-empirical Program Package version*, 2009.

(45) Schäfer, A.; Horn, H.; Ahlrichs, R. Fully optimized contracted Gaussian basis sets for atoms Li to Kr. *J. Chem. Phys.* **1992**, *97*, 2571−2577.

(46) Software Users Guide, v. 6.0, Bruker Analytical X-ray Systems, Madison, WI, 1999.G. M. Sheldrick, SADABAS; Area-Detector Absorption Correction, v. 2.03, University of Gottingen, Germany, 1999; SADABAS, v. 2008.

(47) Sheldrick, G. M. *SHELXT-97*, Prog. Crystal-Structure Refinement, 1997.

(48) Macindoe, G.; Mavridis, L.; Venkatraman, V.; Devignes, M.-D.; Ritchie, D. W. HexServer: an FFT-based protein docking server powered by graphics processors. *Nucleic Acids Res.* **2010**, *38*, W445−W449.

(49) Siddique, H. R.; Mishra, S. K.; Karnes, R. J.; Saleem, M. A novel androgen receptor inhibitor: implications in prostate cancer therapy. *Clin. Cancer Res.* **2011**, *17*, 5379−5391.

https://dx.doi.org/10.1021/acsomega.0c01206
ACS Omega 2020, 5, 15218−15228